Special Issue

Visible-Light Optical Coherence Tomography Angiography for Monitoring Laser-Induced Choroidal Neovascularization in Mice

Ronil S. Shah,[1] Brian T. Soetikno,[1,2,3] Ji Yi,[2] Wenzhong Liu,[2] Dimitra Skondra,[1] Hao F. Zhang,[1,2] and Amani A. Fawzi[1]

[1]Department of Ophthalmology, Feinberg School of Medicine, Northwestern University, Chicago, Illinois, United States
[2]Functional Optical Imaging Laboratory, Department of Biomedical Engineering, Northwestern University, Chicago, Illinois, United States
[3]Medical Scientist Training Program, Northwestern University Feinberg School of Medicine, Chicago, Illinois, United States

Correspondence: Amani A. Fawzi, 645 N Michigan Avenue, Suite 440, Chicago, IL 60611, USA; afawzimd@gmail.com.

RSS and BTS contributed equally to the work presented here and should therefore be regarded as equivalent authors.

Submitted: December 13, 2015
Accepted: March 6, 2016

Citation: Shah RS, Soetikno BT, Yi J, et al. Visible-light optical coherence tomography angiography for monitoring laser-induced choroidal neovascularization in mice. *Invest Ophthalmol Vis Sci*. 2016;57:OCT86–OCT95. DOI:10.1167/iovs.15-18891

Purpose. This study sought to determine the earliest time-point at which evidence of choroidal neovascularization (CNV) could be detected with visible-light optical coherence tomography angiography (vis-OCTA) in a mouse model of laser-induced CNV.

Methods. Visible light-OCTA was used to study laser-induced CNV at different time-points after laser injury to monitor CNV development and measure CNV lesion size. Measurements obtained from vis-OCTA angiograms were compared with histopathologic measurements from isolectin-stained choroidal flatmounts.

Results. Choroidal neovascularization area measurements between the vis-OCTA system and isolectin-stained choroidal flatmounts were significantly different in area for days 2 to 4 postlaser injury, and were not significantly different in area for days 5, 7, and 14. Choroidal neovascularization area measurements taken from the stained flatmounts were larger than their vis-OCTA counterparts for all time-points. Both modalities showed a similar trend of CNV size increasing from the day of laser injury until a peak of day 7 postlaser injury and subsequently decreasing by day 14.

Conclusions. The earliest vis-OCTA can detect the presence of aberrant vessels in a mouse laser-induced CNV model is 5 days after laser injury. Visible light-OCTA was able to visualize the maximum of the CNV network 7 days postlaser injury, in accordance with choroidal flatmount immunostaining. Visible light-OCTA is a reliable tool in both detecting the presence of CNV development, as well as accurately determining the size of the lesion in a mouse laser-induced CNV model.

Keywords: laser-induced choroidal neovascularization, age-related macular degeneration, optical coherence tomography

Age-related macular degeneration (AMD) is a leading cause of blindness in people 50 years of age or older in the United States.[1–3] There are two major subtypes of advanced AMD: dry, or atrophic, and wet, or neovascular. The dry AMD subtype is defined by the deposition of yellow deposits, or drusen, underneath the retinal pigment epithelium (RPE), and progression to RPE loss and geographic atrophy. In the wet AMD subtype, the hallmark is choroidal neovascularization (CNV),[4–6] which can cause exudative leakage, hemorrhage, and fibrosis, leading to photoreceptor damage and, ultimately, irreversible vision loss.[2,4] Although geographic atrophy is a more prevalent cause of vision loss than neovascular AMD, with the use of antiangiogenic therapy, the latter remains the only AMD subtype that is pharmacologically treatable.

Imaging technologies, such as fluorescein angiography (FA), indocyanine green angiography (ICG), and spectral-domain optical coherence tomography (SD-OCT), guide the clinical diagnosis and management of AMD.[3,7] Of the three, SD-OCT is by far the least invasive. Spectral-domain OCT does not require intravenous contrast agents and is also unique in that, by capturing high-resolution depth information, it is inherently cross-sectional, providing three-dimensional (3D) imaging. By contrast, FA and ICG can only provide two-dimensional (2D) images. With these unique advantages, SD-OCT has enabled the study of the intricate, 3D relationship between AMD lesions and the overall structure of the retina.[3,7] One disadvantage of SD-OCT, for the specific purposes of diagnosing neovascular AMD, is that the pathologic vessels of CNV cannot be directly visualized. Because of this limitation, among others, the diagnosis of CNV cannot rely solely on SD-OCT findings[6]; instead, current clinical guidelines require that the structural findings from SD-OCT be interpreted in conjunction with leakage seen on FA in order to conclusively diagnose CNV in AMD.[8]

The laser-induced CNV model in mice, which is one of the most widely used models in neovascular AMD research,[9,10] is an accepted, reliable animal model for neovascular AMD.[10–14] Neovascularization in human AMD arises from an age-related, multifactorial, complex disease state; however, neovascularization in the murine model arises from experimental laser injury. The RPE, with its many darkly colored granules of melanin and

other chromophores, absorbs the laser energy, which results in a localized, thermal rupture of Bruch's membrane, followed by a cascade of inflammatory factors and a self-limited, proangiogenic process.[15,16] Historically, experimental CNV has been studied in vivo, with FA, or ex vivo, with choroid flatmount preparation.[11] Spectral-domain OCT has also been used to visualize CNV formation[11,17] ; however, as discussed previously, this method does not allow direct visualization of the vessels in the neovascular complex.[18]

Recent improvements in both hardware and software have led to the development of OCT angiography (OCTA).[18,19] Unlike SD-OCT, OCTA is sensitive to motion contrast, enabling 3D visualization of blood flowing within vascular networks. Moreover, OCTA allows 3D visualization of pathologic CNV in AMD without the administration of intravenous contrast agents.[18,20,21] Optical coherence tomography angiography volumes can be segmented according to the different layers of the retina and choroid, such that vasculature can be measured in each separate layer, visualized in cross section, or volumetrically reconstructed.[18] This 3D visualization enables the discrimination of abnormal neovascular tissue from the surrounding tissues allowing a more precise localization of CNV.[18,22] Historically, near-infrared (NIR) light has been used in OCT technology; however, our group has recently developed visible-light OCT (vis-OCT), which uses a broad-spectrum light source that is centered in the visible wavelength.[23] Because of the shorter wavelengths, a visible-light source provides higher axial and lateral resolution for OCT than NIR light source.[23] In addition to improved imaging resolution, the visible light spectrum makes it feasible to examine oxygen saturation within the living retina, providing functional information.[24] Recently, we extended the applications of vis-OCT to angiography (vis-OCTA), to examine the retinal vasculature in vivo.[24–26]

In this study, for the first time, we used vis-OCTA to image laser-induced CNV in mice. To best visualize the lesions, we developed an image processing protocol, which removes imaging artifacts and enhances the contrast of the lesion using color-coding. By monitoring laser-induced CNV lesions at different points in time and comparing vis-OCTA with ex vivo stained flatmounts, we were able to determine the earliest time point at which vis-OCTA can detect CNV.

Methods

Animals

All animal studies followed the guidelines established by the ARVO Statement for the Use of Animals in Ophthalmic and Visual Research as well as those set by the Northwestern University Institutional Animal Care and Use Committee (Chicago, IL, USA). Twenty-five adult mice aged 4 to 8 weeks of mixed background were used for this study. Over the course of the experiment, mice were euthanized at predetermined time-points based on the data set that was to be examined (day 2 post laser, day 3 post laser, etc.). For laser injury procedures, anesthesia was achieved via intraperitoneal injection of 2,2,2-tribromoethanol (Avertin; 20mg/kg; Sigma-Aldrich Corp., St. Louis, MO, USA) to minimize cataract formation.[27]

During imaging procedures, mice were placed on a custom-made mouse holder allowing fine manipulation of their position in three dimensions. Anesthesia during imaging and during the perfusion staining procedure performed immediately after imaging was achieved via an intraperitoneal injection of a xylazine (10 mg/kg) and ketamine (87 mg/kg) cocktail. Pupils were dilated with 1% tropicamide solution and kept hydrated with artificial tears (Alcon Laboratories, Ft. Worth, TX, USA).

Laser-Induced CNV

We performed laser photocoagulation using an argon 532-nm laser (IRIDEX Oculight GLx, Mountain View, CA, USA) attached to a slit-lamp delivery system (Carl Zeiss 30SL-M, Jena, Germany). To flatten the cornea and allow visualization of the retina, a glass coverslip with a drop of artificial tear solution was gently placed on the surface of the mouse eye.[28] Laser spots (75-μm spot size, 100-ms duration, 100-mW power) were delivered at 3, 6, 9, and 12 o'clock positions around the optic nerve of both eyes of each animal. Lesions that resulted in "bubble" formation, indicating rupture of Bruch's membrane, were deemed successful. Lesions that did not meet this criterion, or resulted in hemorrhage, were excluded from further analysis.

Visible-Light Optical Coherence Tomography Angiography

Our custom-built vis-OCT imaging system is similar to most other SD-OCT imaging systems, except for the light source, which used a supercontinuum laser (SuperK EXTREME EXW-6; NKT Photonics, Birkerød, Denmark) with a spectrum from 500 to 620 nm.[24,25] A detailed description of the imaging system can be found in a study by Yi et al.[24] Our system has a fast scanning axis and a slow scanning axis. For the fast scanning axis, A-lines were acquired at 50 kHz. Using our custom-built vis-OCT system, we obtained 3D structural images, covering a 0.92×0.92 mm^2 area on the mouse retina. The lateral and axial resolution for this system is approximately 15 μm and 1.7 μm, respectively. A set of glass plates in the reference arm compensated for dispersion introduced by the optical components of the system. Dispersion introduced by the eye was compensated for in postacquisition data processing.

To better visualize the CNV lesion, we employed vis-OCTA, which uses the same imaging system as vis-OCT, but requires a modified scanning pattern and additional post processing of the imaging data. Our vis-OCTA scanning pattern requires that five B-scans be acquired at each position along the slow scanning axis.[25] After image acquisition, the five B-scans are post processed using a phase-sensitive decorrelation algorithm to produce a 3D angiography volume, whose signal represents motion contrast from flowing blood.[29] Angiograms were also motion-corrected for bulk image shift, axial global phase fluctuations, and lateral global phase fluctuations.[30] The relationship between the OCTA decorrelation signal and velocity is nonlinear,[31] and may be affected by the pulsatile nature of blood flow in living subjects. Therefore, OCTA images can help visualize moving blood, but does not provide quantitative measurements of the velocity of blood. Further details of the angiography and signal processing algorithms can be found in a study by Chen et al.[25]

Image Processing for Visualizing CNV

Building upon our experience with structural and functional applications of vis-OCT,[19,24–26,32,33] we developed an imaging and data processing protocol for vis-OCTA of laser-induced CNV. The image processing protocol for visualizing CNV consists of three major steps: flattening the vis-OCTA volume to a reference surface, performing a maximum amplitude projection (MAP), and color-coding the MAP based on depth.

Due to the natural curvature of the retina, the signals within vis-OCT and vis-OCTA volumes are not flat, making it difficult to isolate the CNV lesion for the purposes of visualization. Therefore, to flatten the vis-OCTA volumes, we first generated a reference surface from the structural vis-OCT volumes. For each A-line in the vis-OCT volume, we determined the z-positions of the first maximum signal (i.e., the inner limiting

Investigative Ophthalmology & Visual Science

membrane [ILM]) and the last maximum signal (i.e., the Bruch's membrane). We then averaged these z-positions to obtain an approximate reference surface, representing the middle of the retina. Some areas of the image had low signal-to-noise ratio, making surface detection difficult; therefore, we performed 3D interpolation to fill these areas. Finally, to achieve a flattened vis-OCTA volume, we shifted each A-line in the volume by the z-positions of the reference surface.

Maximum amplitude projections enable the visualization of 3D volumes in a 2D format. If we denote a 3D volume (whether it be a vis-OCT or vis-OCTA volume), then we can mathematically define its MAP along the depth direction as the following:

$$M(x,y) = \max_z I(x,y,z) \quad (1)$$

where the max function returns the maximum value along the z-axis at each (x, y) position. With the vis-OCTA volume flattened, we generated three MAPs for three separate ranges in the z-dimension. The first MAP, which we term the "entire retina" enface angiogram, spanned from the ILM to the choroid. The second MAP, which we term the "inner retina" angiogram, spanned from the ILM to the outer plexiform layer and outer nuclear layer (OPL-ONL) junction. The third MAP, which we term the "outer retina" angiogram, spanned from the OPL-ONL junction to the choroid. To eliminate mirror image artifacts from superficial vessels from the outer retina angiogram, we subtract the inner retina angiogram from the outer retina angiogram, turning bright areas, where artifacts are present, to dark areas. This method appears to be similar to the one employed by Jia et al.[21]

When the MAPs were performed, we also saved the z-position of the location of the maximum amplitude. Using the same notation for a 3D volume as above, the depth information can be extracted using the following equation:

$$D(x,y) = \operatorname{argmax}_z I(x,y,z). \quad (2)$$

From this information, we were able to color code each pixel based on depth. This process provided an improved contrast to the vessels of the CNV, which aided our graders in determining the CNV area from vis-OCTA. CNV lies above the plane of the choroid; therefore, the CNV was colored red or yellow, while the deeper choroidal structures were colored blue and green.

Choroidal Flatmount Preparation and Isolectin Staining of CNV Lesions

After vis-OCTA imaging at each of the six time-points, CNV lesions were evaluated postmortem using isolectin stained choroidal flatmounts. Two isolectin stains were used: one that highlights only perfused blood vessels and one that highlights both perfused and nonperfused blood vessels. In order to highlight perfused blood vessels, mice were anesthetized and underwent cardiac perfusion with isolectin GS-IB_4 conjugated with Alexa Fluor 488 (Life Technologies, Carlsbad, CA, USA), as reported previously.[34,35] Here we injected 50 μL isolectin GS-IB_4 conjugated with Alexa Fluor 488 (0.33 mg/mL) into the left ventricle. A flash of blood followed by a visible flow of blood into the syringe indicated successful puncture of the left ventricle and, therefore, success of the cardiac perfusion procedure.[35] Five minutes after the cardiac perfusion, the animals were euthanized, and eyes were enucleated and fixed in 4% paraformaldehyde (PFA) for 30 minutes at room temperature.

In order to highlight both perfused and nonperfused vessels, we subsequently performed postmortem counterstaining with conjugated with Alexa Fluor 594 (IB_4 594, 1:100; Life Technologies, Carlsbad, CA, USA), which binds to all endothelial cells to label all the vasculature. In addition, this stain also highlights microglia and macrophages. The procedure for this staining is described as follows. After the enucleated eyes have been fixed in 4% PFA for 30 minutes at room temperature, they were transferred to PBS at 4°C. The anterior segment and the lens were removed, and the neurosensory retina was carefully separated from the underlying RPE.[36,37] The remaining RPE-choroid-sclera complex was washed with PBS, blocked with 10% normal donkey serum (NDS) in PBS with 0.5% Triton X-100, and then stained with isolectin GS-IB_4 594.[38] Four relaxing radial incisions were made on the RPE-choroid-sclera complex, which was then flatmounted with Prolongold anti-fade reagent (Life Technologies, Eugene, OR, USA) and cover-slipped.

CNV Area Quantification

To calculate the area of the CNV lesions in the vis-OCTA images, two masked graders (RS, BTS) independently delineated the outlines of the CNV lesions, using the lasso tool in ImageJ software (http://imagej.nih.gov/ij/; provided in the public domain by the National Institutes of Health, Bethesda, MD, USA). Then, using ImageJ's area calculation tool, the area was of the CNV lesion was determined and converted from pixel number to physical dimensions (μm^2). The results of the two graders were compared and the correlation coefficients were calculated. Additionally, we constructed a Bland-Altman plot to check for intergrader agreement and to ensure that there was no systematic pattern of bias.

Choroidal flatmounts were evaluated using confocal microscopy (Zeiss LSM Meta 510; Carl Zeiss, Jena, Germany). The only landmarks to judge the extent of the lesion in the z-direction were the top of the CNV lesion and the RPE. Therefore, we acquired an image stack where the first image visualized the top of the CNV lesion and the last image visualized the RPE.[39,40] For each of the CNV lesions, we simultaneously acquired images at the two isolectin B4 wavelengths. All sections were approximately between 20- to 25-μm thick. Then, an area 20 to 25 um above the RPE was demarcated. This area was integrated to create the en face view of the lesion. The MAP of the confocal microscopy z-stack was performed using ImageJ. The excellent contrast of the obtained stained images allowed the use of an automatic segmentation program to quantify the areas of the lesions. The MAPs were imported into a custom-built, supervised, automated, threshold and area-calculating program in MATLAB 2015 (Mathworks, Natick, MA, USA). This program used a simple thresholding algorithm to obtain a binary mask and subsequently calculate the area of immunofluorescent area. Lesions that could not be adequately visualized due to poor staining with either the perfused IB_4 488 or the whole-mount IB_4 594, and lesions that were damaged during tissue handling were excluded from analysis.

Statistical Analysis

The results are expressed as mean ± SEM, except where noted otherwise. Comparisons were made using a 2-tailed paired t-test. A value of P less than 0.05 was considered significant. All analyses were performed using Graphpad Prism (Version 6; GraphPad Software, San Diego, CA, USA).

Results

Vis-OCTA Image Processing

Figure 1 illustrates the differences between images acquired using vis-OCT, vis-OCTA, and vis-OCTA with postaquisition

Investigative Ophthalmology & Visual Science

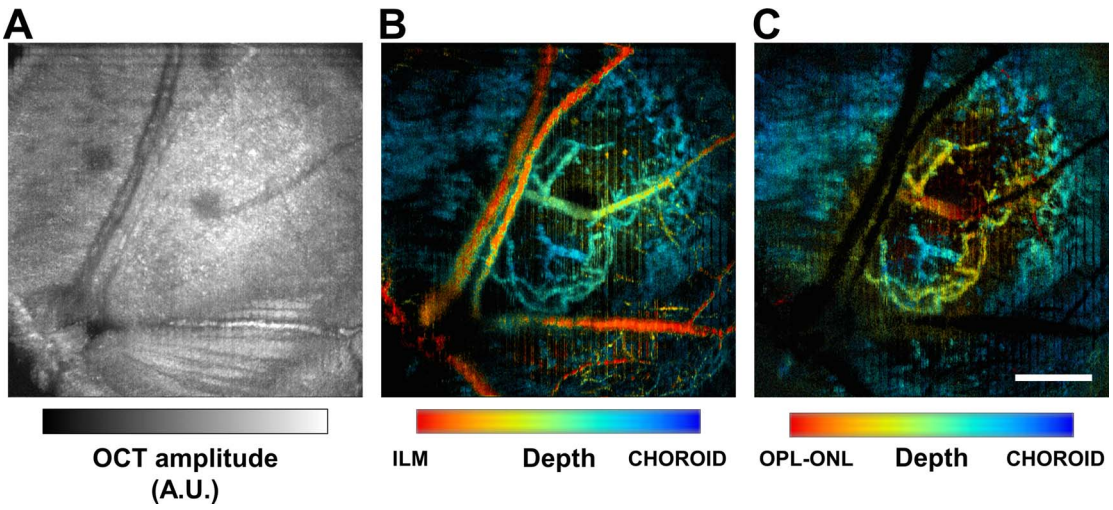

Figure 1. Overview of the visible-light OCT angiography protocol and postaquisition image processing. (**A**) En face MAP of a typical structural vis-OCT volume. The CNV lesion is not visible Arbitrary Units (A.U). (**B**) En face MAP vis-OCT angiography of the same area, revealing the CNV lesion. Image color-coded by depth. (**C**) Final postprocessed outer retina en face angiogram, color-coded by depth. *Scale bar*: 200 μm.

image processing. An example en face vis-OCT MAP, which captured the area surrounding a CNV lesion on postinjury day 7, is shown in Figure 1A. Because vis-OCT images do not reflect motion contrast, only large retinal vessels are visible in the vis-OCT MAP, and no CNV is visible. The vis-OCTA volume can be collapsed into an en face 2D MAP, in the same manner as the vis-OCT volume in Figure 1A. Figure 1B shows an example vis-OCTA MAP for the same CNV lesion corresponding to the same area shown in Figure 1A. The vis-OCTA MAP has been color-coded by depth, with red denoting vessels near the ILM and blue denoting vessels near the choroid. Here we see that there is a large CNV lesion (yellow-green) lying above the choroid. Supplementary Video S1 depicts a depth fly-through movie of the same vis-OCTA volume with pertinent labeling of the vascular layers.

We performed additional postacquisition image processing to enhance the visibility of the CNV lesion. First, instead of performing the MAP along the depth dimension for the entire OCTA volume as in Figure 1B, we performed the MAP on a smaller volume extending from the junction of the OPL-ONL, to the choroid, and modified our depth-color-coding accordingly. Second, we removed OCTA artifacts, which have also been observed by other groups using different angiography techniques.[21,41,42] Vessels in the superficial layers of the retina (e.g., nerve fiber layer) cause a projection artifact onto deeper layers of the retina (e.g., photoreceptor outer segments). Because of these artifacts, it may appear that vasculature is present in deeper layers of the OCTA volume, when there are, in fact, no vessels physically present. Therefore, the interpretation of OCTA images requires caution, especially if no post processing has been performed to remove or diminish these artifacts. We removed these artifacts using a simple subtraction method, detailed in the methods section. Finally, our post-processing yields a color-coded MAP of a CNV lesion alone. An example, corresponding to the lesion shown in Figure 1B (preprocessed), is shown in Figure 1C (postprocessed).

Time Course of Laser-Induced CNV Using Vis-OCTA Compared With Choroidal Flatmounts

In a series of experiments at different points in time after laser injury, we correlated vis-OCTA images of laser-induced CNV choroidal flatmounts stained with endothelial cell marker isolectin B_4. As described in the methods section, two different forms of isolectin staining were used: an intracardiac perfusion method and a total tissue endothelial staining method. The intracardiac perfusion method used green isolectin B_4 488 to highlight perfused blood vessels. The total tissue endothelial staining method used red isolectin B_4 594 to highlight all of the blood vessels (both perfused and nonperfused) as well as supporting microglia and macrophages, in the lesion area.

Using vis-OCTA, we imaged CNV lesions on days 2, 3, 4, 5, 7, and 14 postlaser injury. Example images for each of the six points in time are shown in Figures 2A and 2B. Figure 2A shows cross-sectional structural B-scans through the center of the CNV lesion for each point in time. The vis-OCTA cross-sectional B-scans, shown as red overlays in Figures 2A give a general sense of the CNV blood flow, but can be difficult to interpret due to projection artifacts from superficial vessels in the inner retina. The best visualization, then, appears to be the postprocessed en face view of the CNV lesion, as shown in Figures 2B. For easier visual comparison between the vis-OCTA en face views and the stained flatmounts, we cropped the vis-OCTA images to display all images in Figure 2 with the same physical dimensions (except for the depth dimension of the B-scans). Figure 2C shows corresponding confocal microscopy images of the total tissue endothelial cell staining (red), while Figures 2D show coregistered, merged confocal microscopy images of both the intracardiac perfusion (green) and the total tissue endothelial cell stain (red).

Comparison of CNV Area Between Vis-OCTA and Isolectin-Stained Flatmounts

Choroidal neovascularization lesions area measurements from vis-OCTA images were compared with area measurements from choroidal flatmounts. The area measurements from the two masked independent graders are plotted against each other in Figure 3A. There is good correlation of the area measurements between the graders, which indicates that our vis-OCTA postprocessing protocol provides excellent contrast for robust, easy visualization of the vessels. The measured r value for this data was 0.98, and the R^2 was 0.96, again, indicating excellent correlation. Second, a Bland-Altman plot of the area gradings was created, with the difference in grader measurements on the y-axis and the average of grader measurements on the x-axis (Fig. 3B). No particular trend was found in this plot, suggesting that there is no systematic bias.[43,44] Moreover, the

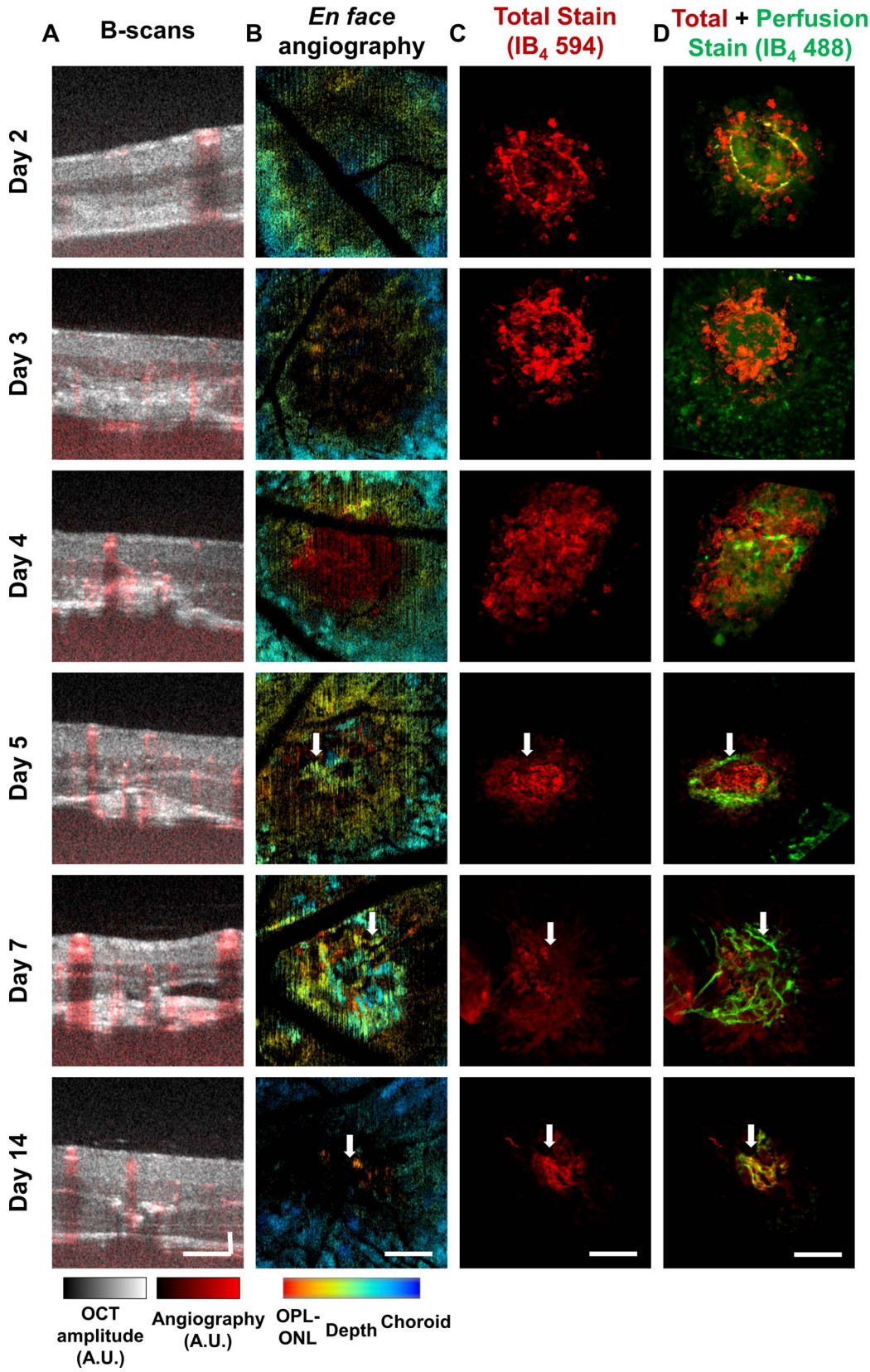

Figure 2. Comparison between in vivo vis-OCT angiography (vis-OCTA) of choroidal neovascular (CNV) lesions and the corresponding ex vivo isolectin B_4 stained flatmounts over time. Each *row* represents a different animal, which was observed at days 2, 3, 4, 5, 7, and 14 after laser injury, respectively. Each column represents a different technique to visualize the CNV lesions. *Column A*: vis-OCT structural B-scans, taken through the center of the CNV lesions, with vis-OCTA B-scans overlaid in *red*. The horizontal dimension matches the other columns, while the vertical dimension does not (because OCT is anisotropic; A.U.). *Column B*: Vis-OCTA of CNV lesions after post processing. Color-coded by depth from the

Investigative Ophthalmology & Visual Science

OPL-ONL to the choroid. The images were cropped from their original size for better comparison with *columns C and D. Column C*: CNV lesions stained after incubation with the endothelial cell marker, isolectin B_4 594 (*red*). Isolectin B_4–stained areas show presence of all vasculature in CNV lesion (as well as accessory macrophages and microglia). *Column D*: CNV lesions stained after cardiac perfusion with isolectin B_4 488 (*green*). Isolectin stained areas (*green*) show only perfused vasculature in CNV lesion. Images show combined images of total staining (IB_4 594, *red*) and perfusion staining (IB_4 488, *green*). *Arrows* show corresponding vessels in OCTA and immunostained images. All *scale bars*: 100 μm.

bias (calculated as the mean of the differences) was small: $3.6e^{-4}$ with a SD of $6.4e^{-3}$. The dashed lines on Figure 3B indicate the 95% confidence interval for the difference in measurements (also known as the 95% limits of agreement), which was −0.012 to 0.013. Given the lack of apparent bias and good agreement between graders, we considered the average of our grader's measurements for the remainder of our analysis.

A comparison between the flatmount and the vis-OCTA CNV area measurements is shown in Figure 4A. We used areas from the total isolectin IB_4-stained flatmounts (red) for comparison with our vis-OCTA areas, because this method is more reflective of the entirety of neovascularization present in the area, and specifically, can detect the immature, non-perfused vascular buds sooner than perfusion staining.[38] The disadvantage of the perfused immunostaining method is that, like the OCTA, it only can provide the area of vessels that are patent enough to have detectable flow. However, total staining can highlight both nascent vessels that are below this flow threshold as well as the mature vessels. Because this metric is a better reflection of the true area of endothelial proliferation, the OCTA area was compared with the total staining. Manual measurements on vis-OCTA show an overall progressive increase of CNV lesion area over time, from day 2 through 7, with CNV area peaking at day 7 after laser injury. The average lesion area decreased between days 7 and 14. Flatmount CNV area calculations showed a similar trend: CNV lesion areas increased during the initial phases from days 2 through 7, with maximum area at day 7, and then subsequently decreased up to day 14.

In order to determine the time-points at which vis-OCTA and the isolectin staining had maximum correlation, the average difference between corresponding vis-OCTA and flatmount CNV areas over time was plotted, as shown in Figure 4B. Statistical analysis showed significant area differences for days 2, 3, and 4, but no significant differences at days 5, 7, and 14, with total IB_4 measuring larger areas than the vis-OCTA angiograms at all points. The earliest time-point vis-OCTA was able to detect CNV without significant difference from the isolectin-stained flatmounts was day 5 postlaser injury.

Discussion

To our knowledge, this is the first time that OCTA has been used to longitudinally monitor laser-induced CNV in mice. While previous studies have examined the structural components of CNV lesions with SD-OCT and fluorescein angiography,[11,17] and compared them with hematoxylin and eosin, immunofluorescence staining, and choroidal flatmounts, these imaging techniques were incapable of OCT angiography. Therefore, these studies could not detect the earliest stages of perfusion of the CNV lesions in the living animal noninvasively with OCTA, and, hence, they were not directly comparable to the stained vascular labeling. As shown in Figure 1 and Supplementary Video S1, we were able to successfully acquire and postprocess vis-OCTA images to reveal laser-induced CNV lesions, with high contrast and free of artifacts. Indeed, vis-OCTA enabled us, for the first time, to visualize the perfusion of CNV lesions at different points in time postlaser injury in vivo (Fig. 2).

Using vis-OCTA, we explored the earliest time-point at which this imaging modality was able to detect CNV. We imaged at various time intervals over a 2-week period to track the overall progress of CNV development, which could be separated into three phases, as previously described.[11,15,45] At day 5 postlaser injury the vis-OCTA system was able to detect the first signs of a perfused lesion, a time-point that coincided with findings of perfusion staining of CNV, which confirms vis-OCTA is detecting flow through the CNV lesion (Fig. 2B). In the following paragraphs, we compare our vis-OCTA results with the isolectin stained flatmount data and to other studies in the literature, and discuss findings of vis-OCTA at each of the experimental time-points. In a temporal fashion, we consider the "early" stage as days 2 and 3 postlaser injury, the "intermediate" stage as days 4 and 5, and the "final" stage as days 7 and 14.

During the early stage of CNV development (days 2 and 3 postlaser injury), the en face angiograms cannot detect the presence of blood flow within lesion's vessels (Fig. 2B). This stage represents an early angiogenesis growth phase,[45] when the CNV lesion is still in its postinjury inflammatory stages. Proangiogenic factors, triggered by the postinjury inflammato-

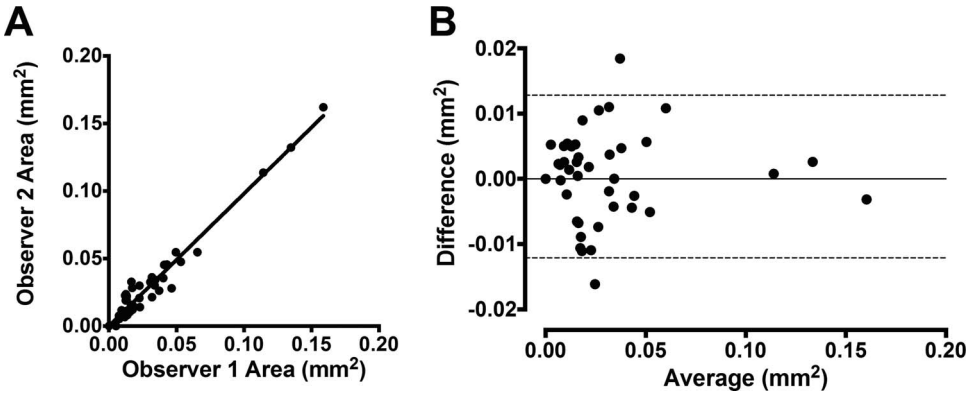

Figure 3. Intergrader reliability for grading of CNV areas in vis-OCTA images. (**A**) Intergrader correlation of measurements. The *r* value was 0.98, and R^2 was 0.96. (**B**) Bland-Altman plot show the agreement of the measurements between the two graders. *Dashed lines* indicate the 95% limits of agreement confidence interval. In several lesions, the graders did not observe any CNV lesion. In these instances, the graders designated the measured area as 0 mm^2. Therefore, for these data points, the difference between the areas was also 0 mm^2.

Investigative Ophthalmology & Visual Science

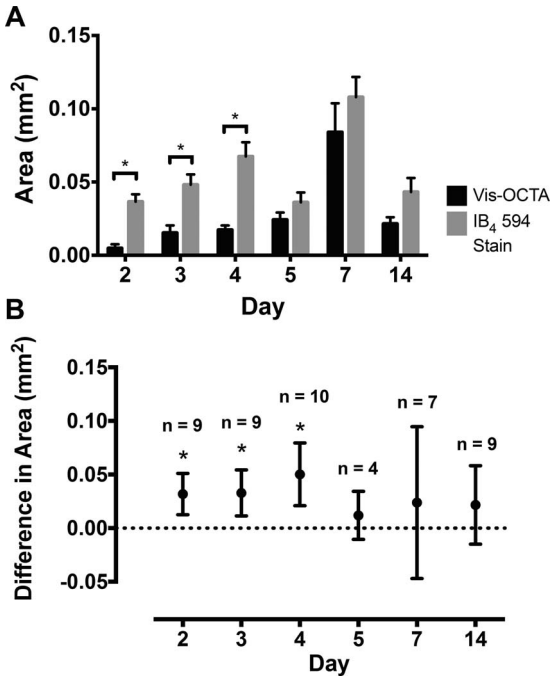

FIGURE 4. Comparison of CNV area on vis-OCTA with areas measured from isolectin-stained flatmounts. (**A**) Average CNV areas for vis-OCTA images and isolectin stained flatmount images. Mean ± SEM. (**B**) Average differences in vis-OCTA areas and flatmount areas over time. Mean ± SD. Two-tailed paired *t*-test with 0.05 significance level cutoff (*). n = number of lesions analyzed, followed by (number of eyes) for each group was as follows: day 2: $n = 9$ (5), day 3: $n = 9$ (3), day 4: $n = 10$ (5), day 5: $n = 4$ (3), day 7: $n = 7$ (6), day 14: $n = 9$ (7).

ry cascade, cause the release of matrix metalloproteinases, which degrade the basement membrane of vessels in the choroid.[46,47] Next, certain endothelial cells are selected to become tip cells, which lead the formation of the new vessels into the outer retina. In order to prevent unorganized growth, cells lateral to the tip cell are muted and, instead, become stalk cells, which make up the tube of the nascent vessels.[46,47] Accessory microglial cells and recruited macrophages are also present to aid the organization and expansion of the new vessels.[48–50] Altogether, the CNV at this early stage has not developed many vessels with fully formed lumens.[38,46,51] Therefore, we hypothesized that at this early stage there would be little to no detectable flow on OCTA within the area of the CNV lesion. Indeed, the vis-OCTA en face angiograms of the CNV lesions (Fig. 2B) reveal a dark circular area at the location of the laser injury, distinct from the surrounding normal retinal and choroidal vasculature. No vessels are visible within this dark area, meaning that CNV could not be detected with vis-OCTA at this stage. In addition, the structural OCT B-scans demonstrate the butterfly-shaped lesion of laser injury, but the overlaid angiography signals showing no evidence of flow in the lesion (Fig. 2A). Furthermore, Figure 4B shows a large average difference in measured area between vis-OCTA and total isolectin staining, which further illustrates the undetectable nature of CNV at this early stage.

Corresponding retinal flatmounts stained with red IB_4 594 (Fig. 2C) show areas of dense hyperfluorescent circular areas without noticeable lumens, representing budding, naïve blood vessels, immature sprouting stubs of endothelial cells, and associated support microglia.[46] Isolectin B_4 specifically targets a-D-galactosyl residues, which are present on many cells involved in the early angiogenic process, including endothelial cells, microglia, and macrophages.[49,50,52,53] Therefore, the presence of staining at this stage is not surprising, given that these cells are known to play a part in early vessel formation and inflammation. Also important to note is that due to multiplicity of cells stained by isolectin B_4, the isolectin stained CNV lesion may be artificially larger, giving the appearance of a more robust lesion than detected by the vis-OCTA system. The green intracardiac injection staining with IB_4 488 reflects perfused blood vessels. Interestingly, the day 2 lesion shows colocalization of both red total tissue isolectin staining and green perfusion staining in a ring-like structure around the laser crater. According to previous studies, this ring-like structure does not indicate formed vessels, but rather represents an auto-fluorescent myofibroblasic scaffold that forms after laser injury.[38,51] Because the blood vessels are still in their naïve nonpatent and nonperfused forms at this early time point, it is not surprising that no definite staining of vessel-like structures is observable. Moreover, the green perfusion staining that is observable in the area of the lesion could represent leakage of dye from these newly formed immature vessels into the lesion. The day 3 lesion is very similar to the day 2 lesion in character, except has an increased area of staining correlating with an increase in CNV complex area.

During the intermediate stage of CNV development (days 4 and 5 postlaser injury), the en face angiograms can detect the presence of blood flow within lesion vessels (Fig. 2B). On the OCTA angiogram, the previous dark circular area of the CNV lesion from the early stage has been replaced by small areas of bright signal scattered throughout; however, an organized vascular network is not evident. Moreover, the flow signal overlaid onto cross-sectional B-scans reveals vascular flow in the area of laser injury, demonstrated by the small red patches of angiography signal near the laser-induced disruption (Fig. 2A). Furthermore, area analysis shown in Figures 4A and 4B for these time-points shows a close matching of area between vis-OCTA and isolectin staining, especially at day 5, when the differences in areas no longer become statistically significant between the two measurements. Corresponding total tissue (red) flatmounts show further development of blood vessels past the initial budding seen in the previous time points, including some with tubular structure, without evidence of a completely formed network, in accordance with the vis-OCTA observations (Fig. 2C). Intracardiac perfusion staining (green) showed a greater degree of overlap between total tissue and perfusion staining compared with the early phase lesions, suggesting maturation of tubular vasculature; however, the majority of vessels still do not appear to be fully interconnected as a mature network (Fig. 2D). At the cellular level, by this point the tip cells have extended outward and the stalk cells have established lumen in the new vessels and perfusion has begun.[46,47] The vascular network will continue to grow until it reaches a peak size and creates an interconnected web of vessels, which, in our study, occurred 7 days after laser injury. In our study, we were able to visualize CNV with the vis-OCTA system at the same time-point at which perfusion isolectin staining demonstrated tubular formed vasculature: 5 days postlaser injury. We concluded that this time point was when the two modalities overlapped because of the lack of statistically significant difference in their area measurements and qualitatively, this is when the image produced by vis-OCTA CNV visualization began to definitively resemble the one obtained from isolectin flatmounts. Although perfusion of the lesion began at the day 4 time-point, a finding agreeing with previous experiments that detected flow via fluorescein isothiocyanate (FITC) dextran perfusion,[38] we believe that the day 5 time-point is when the vis-OCTA system definitively detected the lesion.

At the final stage of CNV development (days 7 and 14 postlaser injury), the vis-OCTA system is able to detect a fully formed, perfused vascular lesion (Fig. 2B). The imaged area shows brightly detectable flow signal, with clearly visualized mature network of interconnected vessels. The angiography overlay B-scan (Fig. 2A) supports this, as this B-scan has the greatest concentration of flow signals compared with other time-points. Flatmount analysis of the lesion also demonstrates a fully formed network (Fig. 2C). Intracardiac perfusion (green) staining shows clear overlap between mature vessels with OCTA flow and flatmounted vessels (Fig. 2D). This indicates that the flatmount IB_4 staining of all endothelial cells in the laser lesion is consistent with the staining highlighted by the perfused IB_4 of blood vessels, which have flow. By day 14, however, substantial lesion regression has occurred, as shown by the reduced area from day 7 in Figure 4A. By inspection, since Figures 2C and 2D are arranged with the same physical dimensions, we see that the red immunostained flatmount shows a smaller-sized lesion than day 7. Although evidence of perfusion is still present (Fig. 2D), decreased lesion size and vascular character resembles those of the intermediate stage. Lesion regression is thought to be primarily driven by reactive RPE that envelops the CNV lesion and absorbs the accumulated subretinal fluid from the leaky, aberrant vessels.[54] Furthermore, the RPE may initiate a wound healing response (e.g., platelet derived growth factor, epidermal growth factor, hepatocyte growth factor) to control the size of the CNV lesion.[15,51,54–57] Another possible mechanism is that the RPE cells could envelope the abnormal vessels in the lesion; a histopathologic study has shown that intact RPE cells proliferate in a papillary pattern around the periphery of the CNV lesion, from areas of healthy, undamaged RPE cells, and slowly grow toward the center of the lesion, enveloping the abnormal vessels.[54] Moreover, using fluorescein angiography, the investigators were able to demonstrate the disappearance of leakage from the CNV site.[54]

Although vis-OCTA and NIR OCTA were not explicitly compared in this study, we will briefly discuss some of the potential theoretical advantages and disadvantages of the two modalities. The two major advantages of using a vis-OCT system are greater imaging resolution and functional measurement of oxygen saturation of hemoglobin. With its shorter wavelength, visible light-OCT enables greater axial resolution and lateral resolution of the retina compared with NIR-based OCT, allowing more detailed images of specific retinal structures, or in this case, angiograms of choroidal neovascularization.[32] Although not performed in this study, the additional benefit of functional imaging with vis-OCT remains to be demonstrated for laser-induced CNV, as it is currently unknown whether oxygen levels play a role in this disease. Interestingly, vis-OCT has recently been demonstrated to measure relative choroidal oxygen saturation values in rodents, which suggests that future studies with vis-OCT could explore this potential area.[32] One major drawback of vis-OCTA versus NIR-OCTA is that, due to higher light absorption in the visible spectral range, the depth of penetration is lower than that of NIR-OCTA. However, based on a preliminary study characterizing the vis-OCTA system in human subjects, our group has imaged the deeper retinal layers and choroid, suggesting neovascular CNV in AMD patients could possibly be visualized.[33] Overall, these comparisons will be important future experiments to explore whether vis-OCTA can provide additional clinically useful information over its NIR counterpart.[8,33]

There were some limitations to the imaging performed in this study. The OCTA signal can be blocked by hemorrhage or opacities in the eye.[58] In addition, all angiography techniques have a minimum detectable flow threshold, primarily determined by the signal-to-noise ratio of the system. If the flow signals at days 2 and 3 were below this minimum detection threshold, then no flow would be detectable on days 2 and 3 post laser. Further studies are required to investigate the minimum detectable flow for OCTA. Another limitation is that large overlying retinal vessels can cause projected artifacts, which we removed with image processing but this process may have also removed true CNV flow signals.[21,58] This shadowing artifact may have contributed to the smaller size of CNV detected on OCTA compared with its immunostained counterpart, where confocal microscopy is not subject to shadowing.

For the first time, our study has performed longitudinal monitoring of laser-induced CNV lesions in mice using OCTA. Our structural findings agreed well, in both character and course, with previous findings using NIR-based SD-OCT. The major advantage of this study is that, with the addition of OCTA, we were able to acquire information about the perfusion of CNV lesions, which has heretofore only been characterized either by ex vivo histology or by in vivo contrast-based imaging methods (e.g., FA or ICG). Because vis-OCTA successfully detected flow in the CNV vessels at the same time point as the histologic data, it validates the ability of this technology to accurately reflect changes in vivo. Further supporting this statement, a recent study compared vis-OCTA and FA for the evaluation of murine laser-induced CNV.[22] The study found that vis-OCTA is better than FA at resolving retinal capillaries in healthy rodent eyes, and successfully detects CNV lesions, which were missed by FA.[22] This study, along with ours, demonstrates the potential of vis-OCTA as an emerging technology, which can successfully characterize, both in structure and perfusion, the formation and regression of CNV lesions in the laser-induced CNV model. We envision that vis-OCTA will be a promising tool in characterizing the pathophysiology of CNV in rodents, and ultimately, once the technology matures,[33] it will hopefully provide an additional new tool to study and monitor therapies for neovascular AMD in humans.

Acknowledgments

Supported by National Institutes of Health Grants 1R01EY019951, 1DP3DK108248 (HFZ and AAF), 1R24EY022883 (HFZ) and T32GM008152 (BTS), Macula Society Research Grants (AAF), and National Science Foundation Grants CBET-1055379 and DBI-1353952 (HFZ; Arlington, VA, USA). A postdoctoral fellowship award from the Juvenile Diabetes Research Foundation (JY: New York, NY, USA), and a Howard Hughes Medical Institute graduate student fellowship (WL; Chevy Chase, MD, USA).

Disclosure: **R.S. Shah**, None; **B.T. Soetikno**, None; **J. Yi**, None; **W. Liu**, None; **D. Skondra**, None; **H.F. Zhang**, None; **A.A. Fawzi**, None

References

1. Bressler NM, Bressler SB, Fine SL. Age-related macular degeneration. *Surv Ophthalmol*. 1988;32:375–413.
2. Congdon N, O'Colmain B, Klaver CC, et al. Causes and prevalence of visual impairment among adults in the United States. *Arch Ophthalmol*. 2004;122:477–485.
3. Jager RD, Mieler WF, Miller JW. Age-Related Macular Degeneration. *N Engl J Med*. 2008;358:2606–2617.
4. Campochiaro PA, Soloway P, Ryan SJ, Miller JW. The pathogenesis of choroidal neovascularization in patients with age-related macular degeneration. *Mol Vis*. 1999;5:34.
5. Lim LS, Mitchell P, Seddon JM, Holz FG, Wong TY. Age-related macular degeneration. *Lancet*. 379:1728–1738.

6. Mowatt G, Hernandez R, Castillo M, et al. Optical coherence tomography for the diagnosis, monitoring and guiding of treatment for neovascular age-related macular degeneration: a systematic review and economic evaluation. *Health Technol Assess*. 2014;18:1–254.
7. Regatieri CV, Branchini L, Duker JS. The role of spectral-domain OCT in the diagnosis and management of neovascular age-related macular degeneration. *Ophthalmic Surg Lasers Imaging*. 2011;42(suppl):S56–S66.
8. de Carlo TE, Bonini Filho MA, Chin AT, et al. Spectral-domain optical coherence tomography angiography of choroidal neovascularization. *Ophthalmology*. 2015;122:1228–1238.
9. Grossniklaus HE, Kang SJ, Berglin L. Animal models of choroidal and retinal neovascularization. *Prog Retin Eye Res*. 2010;29:500–519.
10. Pennesi ME, Neuringer M, Courtney RJ. Animal models of age related macular degeneration. *Mol Aspects Med*. 2012;33:487–509.
11. Giani A, Thanos A, Roh MI, et al. In vivo evaluation of laser-induced choroidal neovascularization using spectral-domain optical coherence tomography. *Invest Ophthalmol Vis Sci*. 2011;52:3880–3887.
12. Tobe T, Ortega S, Luna JD, et al. Targeted disruption of the FGF2 gene does not prevent choroidal neovascularization in a murine model. *Am J Pathol*. 1998;153:1641–1646.
13. Ryan SJ. The development of an experimental model of subretinal neovascularization in disciform macular degeneration. *Trans Am Ophthalmol Soc*. 1979;77:707–745.
14. Montezuma SR, Vavvas D, Miller JW. Review of the ocular angiogenesis animal models. *Semin Ophthalmol*. 2009;24:52–61.
15. Miller H, Miller B, Ishibashi T, Ryan SJ. Pathogenesis of laser-induced choroidal subretinal neovascularization. *Invest Ophthalmol Vis Sci*. 1990;31:899–908.
16. Kwak N, Okamoto N, Wood JM, Campochiaro PA. VEGF is major stimulator in model of choroidal neovascularization. *Invest Ophthalmol Vis Sci*. 2000;41:3158–3164.
17. Hoerster R, Muether PS, Vierkotten S, Schroder S, Kirchhof B, Fauser S. In-vivo and ex-vivo characterization of laser-induced choroidal neovascularization variability in mice. *Graefes Arch Clin Exp Ophthalmol*. 2012;250:1579–1586.
18. Jia Y, Bailey ST, Wilson DJ, et al. Quantitative optical coherence tomography angiography of choroidal neovascularization in age-related macular degeneration. *Ophthalmology*. 2014;121:1435–1444.
19. Yi J, Chen S, Backman V, Zhang HF. In vivo functional microangiography by visible-light optical coherence tomography. *Biomed Opt Express*. 2014;5:3603.
20. Srinivasan VJ, Jiang JY, Yaseen MA, et al. Rapid volumetric angiography of cortical microvasculature with optical coherence tomography. *Opt Lett*. 2010;35:43–45.
21. Jia Y, Bailey ST, Hwang TS, et al. Quantitative optical coherence tomography angiography of vascular abnormalities in the living human eye. *Proc Natl Acad Sci U S A*. 2015;112:E2395–E2402.
22. Liu W, Li H, Shah RS, et al. Simultaneous optical coherence tomography angiography and fluorescein angiography and fluorescein angiography in rodents with normal retina and laser induced choroidal neovascularization. *Opt Lett*. 2015;40.
23. Yi J, Li X. Estimation of oxygen saturation from erythrocytes by high-resolution spectroscopic optical coherence tomography. *Opt Lett*. 2010;35:2094–2096.
24. Yi J, Wei Q, Liu W, Backman V, Zhang HF. Visible-light optical coherence tomography for retinal oximetry. *Opt Lett*. 2013;38:1796–1798.
25. Chen S, Yi J, Zhang HF. Measuring oxygen saturation in retinal and choroidal circulations in rats using visible light optical coherence tomography angiography. *Biomed Opt Express*. 2015;6:2840–2853.
26. Soetikno BT, Yi J, Shah R, et al. Inner retinal oxygen metabolism in the 50/10 oxygen-induced retinopathy model. *Sci Rep*. 2015;5:16752.
27. Lambert V, Lecomte J, Hansen S, et al. Laser-induced choroidal neovascularization model to study age-related macular degeneration in mice. *Nat Prot*. 2013;8:2197.
28. Shah R, Soetikno B, Lajko M, Fawzi AA. A Mouse model for laser induced choroidal neovascularization. *J Vis Exp*. In press.
29. Jia Y, Tan O, Tokayer J, et al. Split-spectrum amplitude-decorrelation angiography with optical coherence tomography. *Opt Express*. 2012;20:4710–4725.
30. Lee J, Srinivasan V, Radhakrishnan H, Boas DA. Motion correction for phase-resolved dynamic optical coherence tomography imaging of rodent cerebral cortex. *Opt Express*. 2011;19:21258–21270.
31. Tokayer J, Jia Y, Dhalla AH, Huang D. Blood flow velocity quantification using split-spectrum amplitude-decorrelation angiography with optical coherence tomography. *Biomed Opt Express*. 2013;4:1909–1924.
32. Chen S, Yi J, Inayat S, Liu W, Cang J, Zhang HF. Measuring absolute microvascular blood flow in cortex using visible-light optical coherence tomography. *Conf Proc IEEE Eng Med Biol Soc*. 2014;2014:3881–3884.
33. Yi J, Chen S, Shu X, Fawzi AA, Zhang HF. Human retinal imaging using visible-light optical coherence tomography guided by scanning laser ophthalmoscopy. *Biomed Opt Express*. 2015;6:3701.
34. Rattner A, Yu H, Williams J, Smallwood PM, Nathans J. Endothelin-2 signaling in the neural retina promotes the endothelial tip cell state and inhibits angiogenesis. *Proc Natl Acad Sci U S A*. 2013;110:E3830–E3839.
35. Campbell JP, Merkel AR, Masood-Campbell SK, Elefteriou F, Sterling JA. Models of bone metastasis. *J Vis Exp*. 2012:e4260.
36. McMenamin PG. Optimal methods for preparation and immunostaining of iris, ciliary body, and choroidal whole-mounts. *Invest Ophthalmol Vis Sci*. 2000;41:3043–3048.
37. Claybon A, Bishop AJR. Dissection of a mouse eye for a whole mount of the retinal pigment epithelium. *J Vis Exp*. 2011;48:2563.
38. Campos M, Amaral J, Becerra SP, Fariss RN. A novel imaging technique for experimental choroidal neovascularization. *Invest Ophthalmol Vis Sci*. 2006;47:5163–5170.
39. Sakurai E, Anand A, Ambati BK, van Rooijen N, Ambati J. Macrophage depletion inhibits experimental choroidal neovascularization. *Invest Ophthalmol Vis Sci*. 2003;44:3578–3585.
40. Jawad S, Liu B, Li Z, et al. The role of macrophage class a scavenger receptors in a laser-induced murine choroidal neovascularization model. *Invest Ophthalmol Vis Sci*. 2013;54:5959–5970.
41. Jia Y, Morrison JC, Tokayer J, et al. Quantitative OCT angiography of optic nerve head blood flow. *Biomed Opt Express*. 2012;3:3127–3137.
42. Kim DY, Fingler J, Zawadzki RJ, et al. Optical imaging of the chorioretinal vasculature in the living human eye. *Proc Natl Acad Sci*. 2013;110:14354–14359.
43. Hanneman SK. Design, analysis, and interpretation of method-comparison studies. *AACN Adv Crit Care*. 2008;19:223–234.
44. Giavarina D. Understanding Bland Altman analysis. *Biochem Med (Zagreb)*. 2015;25:141–151.
45. Campa C, Costagliola C, Incorvaia C, et al. Inflammatory mediators and angiogenic factors in choroidal neovascularization: pathogenetic interactions and therapeutic implications. *Mediators Inflamm*. 2010;2010:pii:546826.

Investigative Ophthalmology & Visual Science

46. Carmeliet P. Mechanisms of angiogenesis and arteriogenesis. *Nat Med*. 2000;6:389–395.
47. Potente M, Gerhardt H, Carmeliet P. Basic and therapeutic aspects of angiogenesis. *Cell*. 2011;146:873–887.
48. Caicedo A, Espinosa-Heidmann DG, Pina Y, Hernandez EP, Cousins SW. Blood-derived macrophages infiltrate the retina and activate Muller glial cells under experimental choroidal neovascularization. *Exp Eye Res*. 2005;81:38–47.
49. Checchin D, Sennlaub F, Levavasseur E, Leduc M, Chemtob S. Potential role of microglia in retinal blood vessel formation. *Invest Ophthalmol Vis Sci*. 2006;47:3595–3602.
50. Rymo SF, Gerhardt H, Wolfhagen Sand F, Lang R, Uv A, Betsholtz C. A two-way communication between microglial cells and angiogenic sprouts regulates angiogenesis in aortic ring cultures. *PLoS One*. 2011;6:e15846.
51. He L, Marneros AG. Macrophages are essential for the early wound healing response and the formation of a fibrovascular scar. *Am J Pathol*. 2013;182:2407–2417.
52. Benton RL, Maddie MA, Minnillo DR, Hagg T, Whittemore SR. Griffonia simplicifolia isolectin B4 identifies a specific subpopulation of angiogenic blood vessels following contusive spinal cord injury in the adult mouse. *J Comp Neurol*. 2008; 507:1031–1052.
53. Laitinen L. Griffonia simplicifolia lectins bind specifically to endothelial cells and some epithelial cells in mouse tissues. *Histochem J*. 1987;19:225–234.
54. Miller H, Miller B, Ryan SJ. The role of retinal pigment epithelium in the involution of subretinal neovascularization. *Invest Ophthalmol Vis Sci*. 1986;27:1644–1652.
55. Sugino IK, Wang H, Zarbin MA. Age-related macular degeneration and retinal pigment epithelium wound healing. *Mol Neurobiol*. 2003;28:177–194.
56. Harada C, Mitamura Y, Harada T. The role of cytokines and trophic factors in epiretinal membranes: involvement of signal transduction in glial cells. *Prog Retin Eye Res*. 2006;25:149–164.
57. Xu KP, Yu FS. Cross talk between c-Met and epidermal growth factor receptor during retinal pigment epithelial wound healing. *Invest Ophthalmol Vis Sci*. 2007;48:2242–2248.
58. de Carlo TE, Romano A, Waheed NK, Duker JS. A review of optical coherence tomography angiography (OCTA). *Int J Retina Vitreous*. 2015;1:5.